



Distinct slab interfaces imaged within the mantle transition zone

Xin Wang^{1,2}, Qi-Fu Chen^{1,3}✉, Fenglin Niu^{4,5}✉, Shengji Wei^{6,7}, Jieyuan Ning⁸, Juan Li^{1,3}, Weijun Wang⁹, Johannes Buchen¹⁰ and Lijun Liu¹⁰

Oceanic lithosphere descends into Earth's mantle at subduction zones and drives material exchange between Earth's surface and its deep interior. The subduction process creates chemical and thermal heterogeneities in the mantle, with the strongest gradients located at the interfaces between subducted slabs and the surrounding mantle. Seismic imaging of slab interfaces is key to understanding slab compositional layering, deep-water cycling and melting, yet the existence of slab interfaces below 200 km remains unconfirmed. Here, we observe two sharp and slightly dipping seismic discontinuities within the mantle transition zone beneath the western Pacific subduction zone that coincide spatially with the upper and lower bounds of the high-velocity slab. Based on a multi-frequency receiver function waveform modelling, we found the upper discontinuity to be consistent with the Mohorovičić discontinuity of the subducted oceanic lithosphere in the mantle transition zone. The lower discontinuity could be caused by partial melting of sub-slab asthenosphere under hydrous conditions in the seaward portion of the slab. Our observations show distinct slab–mantle boundaries at depths between 410 and 660 km, deeper than previously observed, suggesting a compositionally layered slab and high water contents beneath the slab.

Oceanic lithosphere forms at mid-ocean spreading centres and descends into the mantle at subduction zones. The subduction process transports chemically differentiated and hydrated rocks into Earth's mantle, producing substantial compositional and thermal heterogeneities¹. The morphology of subducting slabs has been investigated by various seismic tomography studies^{2–4}. However, it remains unclear what happens at the boundaries between the subducting slab and the surrounding mantle (hereafter referred to as slab interfaces).

At shallow depths (<200 km), a variety of seismic reflection studies of subduction zones have identified the upper and/or lower interfaces of subducting slabs, all of which are characterized by sharp seismic velocity discontinuities^{5–8}. At the upper interface of the subducting slab, dehydration of oceanic crust enhances the velocity contrast between the slab and the overlying mantle wedge, as water released from the slab reacts with ultramafic mantle rocks to form hydrous minerals such as serpentine^{6,9}. Even though most of the water is thought to be released from the oceanic crust at depths above 150–200 km, hydrous minerals may persist to greater depths^{9–11} and could potentially contribute to sharp velocity contrasts, as observed down to 500 km atop a slab in central Japan⁸. By storing water in hydrous minerals, such as lawsonite and dense hydrous magnesium silicates, as well as in nominally anhydrous minerals, the slab's upper interface provides a pathway for transporting water deep into the mantle. The slab's lower interface, defined as the boundary between the oceanic lithosphere and the underlying asthenosphere, could be also marked by a sharp seismic velocity discontinuity¹². For example, Kawakatsu et al.⁵ reported an approximately 35° dipping discontinuity at the base of the Pacific

slab in the Japan subduction zone, extending down to 200 km depth. Seismic contrasts across the slab and the underlying asthenosphere have been attributed to the accumulation of partial melt^{5,7}. The detection of partial melt beneath slab is important for understanding the mechanical coupling between the subducting lithosphere and the underlying asthenosphere.

Seismic imaging of both the upper and lower slab interfaces is therefore key to understanding slab dynamics in the mantle, such as compositional layering, deep-water cycling and melting. However, how deep the seismic velocity discontinuities at slab interfaces can extend remains unclear, mainly due to the lack of high-resolution imaging of slab interfaces at depths below 200 km.

Double seismic discontinuities within the mantle transition zone

Here, we study the properties of slab interfaces using the P-wave receiver function (RF) technique¹³, which can capture velocity discontinuities beneath seismic stations. We obtain 67,344 high-quality RF waveforms from 313 regional seismic stations in northeast China (Fig. 1), where the Pacific slab appears to subduct and stagnate^{2–4} within the mantle transition zone (MTZ). We then use the common-conversion-point (CCP) stacking technique¹⁴ to image the MTZ structures (Methods).

Positive-amplitude P-to-S converted phases (Ps) at depths of ~420 km and ~680 km are clearly imaged in the entire region (Fig. 2), representing the global 410 km and 660 km discontinuities. There is a clear negative signal just above 410 km on the CCP images, which has been associated with dehydration melting at the top of a wet MTZ¹⁵. In addition, two phases related to velocity

¹Key Laboratory of Earth and Planetary Physics, Institute of Geology and Geophysics, Chinese Academy of Sciences, Beijing, China. ²Seismological Laboratory, California Institute of Technology, Pasadena, CA, USA. ³College of Earth and Planetary Sciences, University of Chinese Academy of Sciences, Beijing, China. ⁴Department of Earth, Environmental and Planetary Sciences, Rice University, Houston, TX, USA. ⁵State Key Laboratory of Petroleum Resources and Prospecting, and Unconventional Petroleum Research Institute, China University of Petroleum at Beijing, Beijing, China. ⁶Earth Observatory of Singapore, Nanyang Technological University, Singapore, Singapore. ⁷Asian School of Environment, Nanyang Technological University, Singapore, Singapore. ⁸School of Earth and Space Sciences, Peking University, Beijing, China. ⁹Institute of Earthquake Forecasting, China Earthquake Administration, Beijing, China. ¹⁰Department of Geology, University of Illinois Urbana-Champaign, Urbana, IL, USA. ✉e-mail: chenqf@mail.iggcas.ac.cn; niu@rice.edu

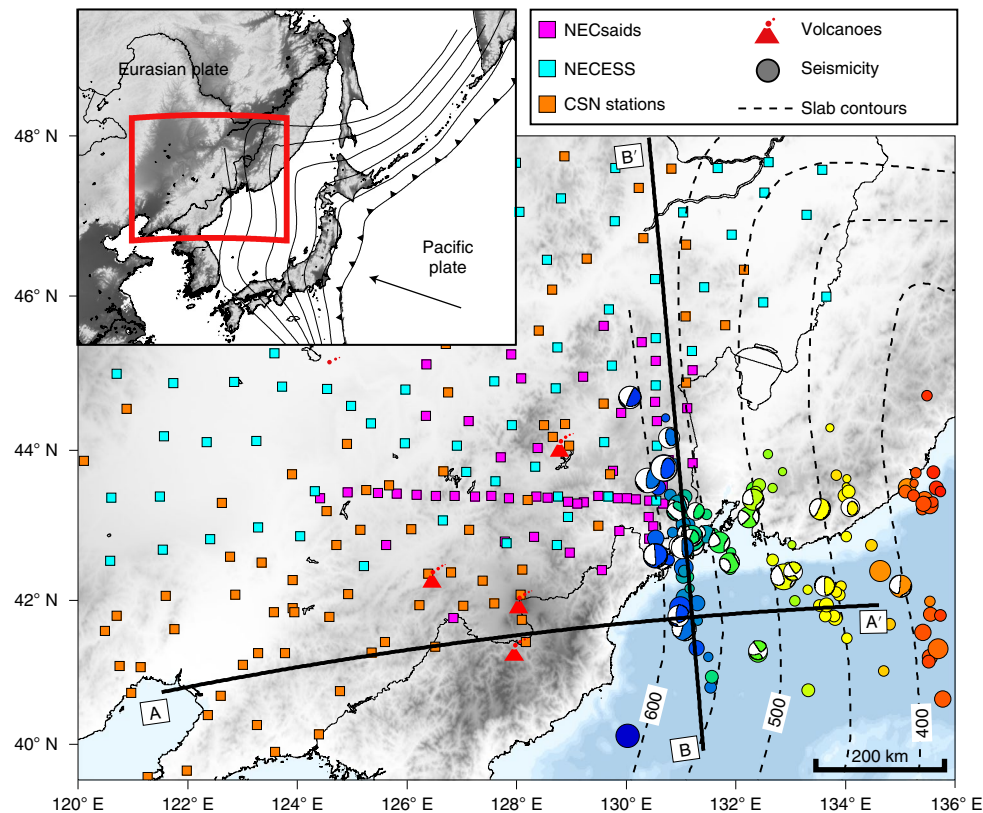


Fig. 1 | Map of the subduction region in northeast China. The squares show the seismic stations used in this study. The thick black lines indicate the locations of the profiles shown in Fig. 2. The black dashed curves show the slab geometry inferred from the distribution of intermediate/deep earthquakes. The dots and beach-balls show the seismicity in this region from the EHB¹⁶ and GCMT (<https://www.globalcmt.org/>) catalogues, respectively, from January 1960 to December 2017. The red triangles indicate the regional Cenozoic volcanoes. NECsaids, Northeast China Seismic Array to Investigate Deep Subduction; NECESS, Northeast China Extended Seismic Array; CSN, China Digital Seismic Network.

discontinuities within the MTZ are observed on the stacked images, and are referred to as phases X1 and X2 (Fig. 2). Phase X1 has a positive amplitude, corresponding to increasing velocity with depth. Phase X2 has a negative amplitude, indicating decreasing velocity with depth. Phases X1 and X2 are approximately parallel and dip by about 25° east of 130°E, then flatten to the west (Fig. 2c). Their locations enclose the hypocentres of deep seismicity¹⁶ and coincide with the upper and lower boundaries of the high-velocity Pacific slab imaged by a recent full-waveform tomographic study⁴. Phases X1 and X2 can be clearly identified throughout the profile BB'—a profile parallel to the strike of the subducting Pacific slab (Fig. 1), indicating that phases X1 and X2 are common features in northeast China (Extended Data Figs. 1–3). Detailed noise analysis and 2D synthetic tests suggest that these two phases are well resolved and are not caused by either the side-lobes in the data processing or reverberations from shallow structures (Supplementary Sections 3–5). A systematic comparison of phases X1 and X2 with the slab-related high-velocity anomalies from tomographic images shows that they are correlated, especially for the dipping section, with a correlation coefficient of up to 0.65 (Methods; Extended Data Fig. 4). Phases X1 and X2 seem to delineate the boundaries between the high-velocity Pacific slab and the surrounding mantle.

Phases X1 and X2 are observed pervasively across the entire study region, with notable lateral variations in amplitudes (Fig. 2), which can be as strong as those of the 410 km (P410s) and 660 km (P660s) discontinuities. The RF amplitudes of phases X1 and X2 decrease with increasing frequency, indicating that they originate from gradual changes in velocities rather than sharp velocity discontinuities^{17,18} (Fig. 3a–d). Forward modelling (Methods; Extended

Data Figs. 5–7) of the frequency-dependent RF waveforms indicates that phases X1 and X2 are well reproduced by velocity jumps of 4–6%, spread over 20–50 km in depth (Fig. 3e). Note that due to the unmodelled three-dimensional velocity heterogeneity effect, the 4–6% velocity contrasts are probably underestimated, and the 20–50 km thickness could be overestimated. To the east of 130°E, phases X1 and X2 dip to the west and seem to have sharper velocity gradients and larger velocity contrasts, as the dipping phases X1 and X2 are clearly visible around 0.75 Hz (Fig. 3d). As a rule of thumb, the velocity gradient thickness of these phases should be less than or equal to half of the wavelength of the incident P waves¹⁹, suggesting that seismic velocity gradients across dipping phases X1 and X2 must occur over a thickness of <10 km.

The origin of phase X1

Our RF results indicate that phase X1 requires a velocity increase of ~4–6% over a depth interval of about 20–50 km located at a depth of about 520 km (Figs. 2 and 3). For the dipping section, the seismic velocity gradient across phase X1 can be as sharp as 10 km, owing to the seismic signals appearing around ~0.75 Hz. Previous observations of discontinuities at depths close to 520 km have been related to the phase transition from wadsleyite to ringwoodite^{20,21} and the exsolution of CaSiO₃ perovskite from garnet²². However, mineral physics experiments and first-principles calculations suggest that the S-wave velocity contrast between wadsleyite and ringwoodite is most probably below 5% (refs. ^{23,24}) and needs to be further scaled down in proportion to their volume fractions in peridotitic rocks (50–60 vol%). Although thermodynamic modelling indicates that the S-wave velocity contrast across the wadsleyite–ringwoodite

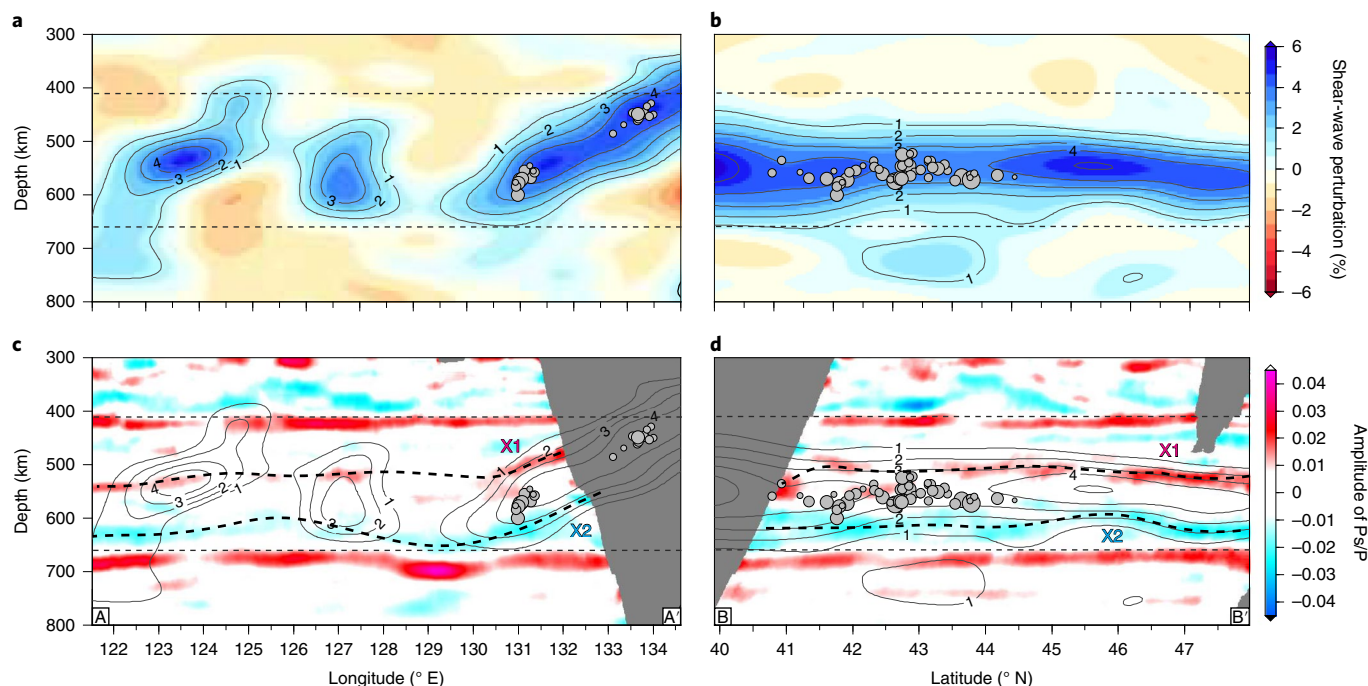


Fig. 2 | Slab interfaces imaged at MTZ depths are consistent with slab geometry inferred from seismicity and full-waveform tomography images.

a, b, The full-waveform tomographic images from Tao et al.⁴ along profiles A (**a**) and B (**b**). The subducting Pacific slab is highlighted by positive velocity anomaly contours. The grey dots show the seismicity from the EHB catalogue¹⁶. **c, d**, The receiver function stacking images constructed using a low-pass filter of -0.35 Hz along profiles A (**c**) and B (**d**). The imaged interfaces within the MTZ are highlighted by the dashed lines, with X1 and X2 marking the positive and negative amplitudes, respectively. The earthquakes and velocity anomaly contours in **a** are also shown in **b**. The global 410 km and 660 km seismic discontinuities are given as thin horizontal dashed lines. The velocity contrast across the discontinuity is given by the amplitude ratio of P-to-S converted phases and the direct P wave (P_s/P).

phase transition increases with decreasing temperature^{25,26}, and could reach the observed values of 4–6%, these calculations also suggest that this phase transition has a very large Clapeyron slope of $2\text{--}5\text{ MPa K}^{-1}$ (refs. ^{23,27}), resulting in much shallower phase change depths that are inconsistent with the observed depths of phase X1 (Extended Data Fig. 8). Thus, it is difficult to explain phase X1 using the wadsleyite–ringwoodite phase transition.

We also test whether phase X1 could be caused by the thermal gradient of a subducting slab, as there is a distinct temperature difference between the slab and the surrounding mantle^{2–4}. We consider a typical subduction geothermal model in the northwest Pacific subduction zone²⁸, where the coldest core of the slab is about 1,000 K cooler than the surrounding mantle, a temperature difference much greater than current seismological observations would suggest (Supplementary Section 6). We estimate the two-dimensional velocity anomalies due to the thermal effect using a temperature–velocity relationship²⁹, resulting in a maximum S-wave velocity anomaly of $\sim 8\%$. By considering the effect of the dipping slab on RF waveforms, we use three earthquakes with a P-wave incidence from the slab downdip direction to explore the maximum possible RF energy in the CCP stacking image. We generate the synthetic seismograms based on a 2D finite difference method³⁰, and then compute the synthetic RFs and construct the CCP stacking image in the same manner as the real data. Our 2D synthetic tests indicate that the temperature gradient in recent geothermal models is too broad (larger than 100 km) to produce enough seismic energy in the high frequencies to match our RF observations (for example, Fig. 3).

The subducting slab is generally composed of a basaltic oceanic crust at the top (~ 6 km) and underlying layers of harzburgite (~ 25 km) and lherzolite (~ 50 km)³¹. Most recent experimental estimates show that eclogite has substantially lower velocities

(a shear-wave velocity (v_s) difference of about -5%) than harzburgite at temperature–pressure conditions of the MTZ³², suggesting that the velocity contrast at the Moho of the subducting oceanic lithosphere remains positive, whereas velocity differences between the oceanic crust and the mantle above are much smaller (Fig. 4c). The interface between a basaltic layer and the underlying depleted harzburgitic mantle lithosphere within the MTZ could give rise to velocity gradients that match our RF observations of phase X1. The sharpness of this interface would depend on the extent of deformation and thermochemical diffusion of the basaltic layer, which would partly erase the sharp lithological contrast and broaden and blur gradients in physical properties. Therefore, we propose a buried Moho as an interpretation of phase X1. Although such a scenario was proposed earlier on the basis of contrasts in the physical properties between MTZ minerals²³, our study provides direct observational evidence in support of this interpretation. Under extremely water-rich and cold conditions, phase X1 could be also caused by the existence of dense hydrous magnesium silicates at the base of the mantle wedge at MTZ depths (Fig. 4b), as suggested by Iwamori⁹ and Tonegawa et al.⁸.

The origin of phase X2

Our RF analysis suggests that phase X2 is similar in magnitude and sharpness to phase X1 but with an opposite polarity. The flattened section of phase X2 corresponds to a shear-wave velocity reduction of 4–6% within a 20–50 km depth interval located around 630 km depth (Fig. 3), whereas the dipping section of phase X2 is much sharper, with a velocity gradient restricted to less than 10 km. Similar velocity reductions (negative RF signals) above the 660 km discontinuity have previously been observed beneath South Africa³³, North America³⁴, Northeast Asia³⁵ and even globally³⁶. They were interpreted as a low-velocity layer made of recycled

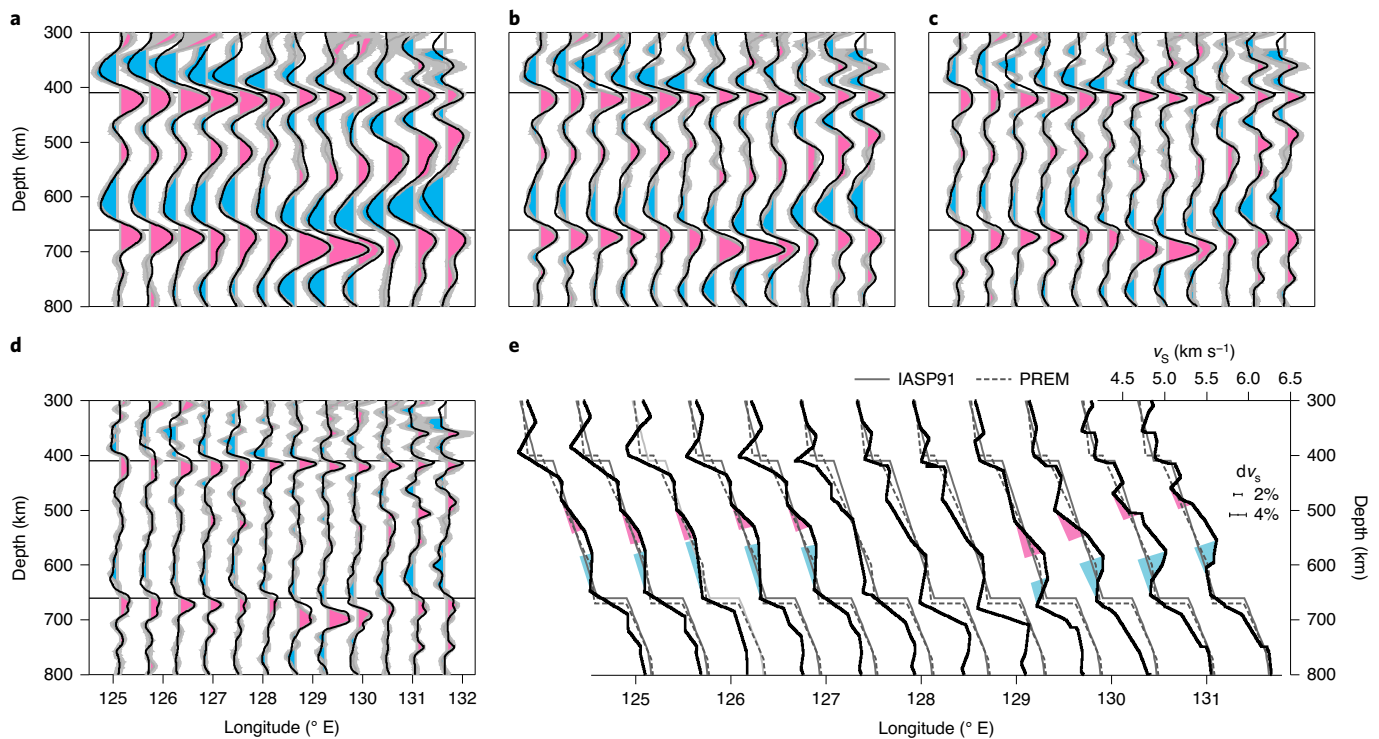


Fig. 3 | Velocity perturbations across phases X1 and X2 inferred from multi-frequency waveform modelling are large, around 4–6%. a–d, Multi-frequency RF waveform modelling with central frequencies of -0.25 Hz (**a**), -0.35 Hz (**b**), -0.5 Hz (**c**) and -0.75 Hz (**d**). Observations are shown as colour-coded waveforms, with the grey shading showing the uncertainties in the RF observations. The black lines show the synthetic RF waveforms, providing good fits to the observed RFs. **e,** Optimal shear-velocity models obtained from multiple-frequency RF modelling. For comparison, the 1D shear-velocity models from IASP91⁴⁹ and PREM⁵⁰ are shown as solid and dashed grey lines, respectively. The magenta and blue shaded regions highlight the velocity changes across phases X1 and X2, respectively.

oceanic crust gradually accumulating at the base of the MTZ³³. This interpretation is supported by recent experimental studies that suggest the existence of substantial velocity contrasts between basalt and a harzburgitic-rich lower MTZ^{29,32}. The basaltic layer of a slab is denser than other slab components and the ambient mantle at all depths to 660 km (ref. ³⁷) and therefore could be detached from the slab and be partially trapped around the 660 km discontinuity. In contrast, the harzburgite layer of the slab, which has similar density to the ambient mantle, may have accumulated at shallower MTZ depths over time^{29,32,37,38}. An accumulation of basaltic materials within a harzburgite-dominated lower MTZ could give rise to local velocity reductions (Fig. 4c). Thus, phase X2 could represent the velocity contrast between the harzburgite-rich lower MTZ and the detached basaltic oceanic crust located underneath.

However, the aforementioned scenario is unable to explain the dipping section of phase X2 (Fig. 2c), as the dipping section is not spatially correlated with the existence of basalt (Extended Data Fig. 9). Phase X2 also cannot be explained by the thermal structure of the slab, as the velocity gradient caused by thermal diffusion at the base of slab is not sharp enough to produce strong negative RF signals, especially at high frequencies³⁵. Given the good spatial correlation of phase X2 and the slab geometry, we interpret the dipping section of the lower interface as partial melts located directly beneath the subducting Pacific slab (Fig. 4b).

Kawakatsu et al.⁵ proposed a partially molten asthenosphere beneath the Japan subduction zone, where the RF studies observed a sharply dipping seismic velocity discontinuity down to 200 km depth (Fig. 4a). Similar thin, prominent, low-velocity layers located immediately below the subducting lithosphere are also visible in New Zealand⁷ and the Cascadia subduction zone³⁹, and are attributed

to the sub-slab partial melts and/or volatiles. The sub-slab partial melts and/or volatiles could be transported and dragged downward by the subducting lithosphere⁴⁰. However, the slab-entrained partial melts/volatiles are expected to solidify at the depth of the MTZ to form a sub-slab layer of eclogite. As eclogite at MTZ depths has a seismic signature roughly similar to the surrounding mantle (lherzolite and pyrolyte), this layer is thus seismically invisible. Tang et al.⁴¹ proposed that the Pacific plate could trap a hot and buoyant sub-lithospheric mantle, which could be entrained by the subduction process and provide the source for the Changbaishan volcanism in northeast China. This scenario is also suggested by geodynamic modelling⁴². In fact, a hot sub-lithosphere is indicated by elongated, dipping, low-velocity anomalies right below high-velocity slabs shown in tomographic images^{2–4} (Extended Data Fig. 10), as well as the depressed 410 km discontinuity behind the subducting Pacific plate⁴³. Both numerical modelling and seismic observations suggested that hot and sub-lithospheric mantle can easily reach the MTZ. If the MTZ is wet, the excessive heat could trigger local melting below the slab. The MTZ in the western Pacific subduction zone is particularly wet, with water contents as high as ~ 0.5 – 1.0 wt% reported from electromagnetic studies^{44,45}. Local concentrations of water near the slab may exceed the MTZ water solubility (0.76 wt%; ref. ⁴⁶), generating partial melts. Such partial melting substantially reduces shear-wave velocities and represents one of the possible mechanisms for the observed velocity reduction beneath the slab. In this scenario, the sub-slab material is relatively hot, and the depressed 660 km discontinuity in the region could then be mainly attributed to non-thermal effects, such as the slab kinematic effects, the majorite garnet phase transition⁴⁷ and/or the high water content in ringwoodite¹¹. We also want to point out that

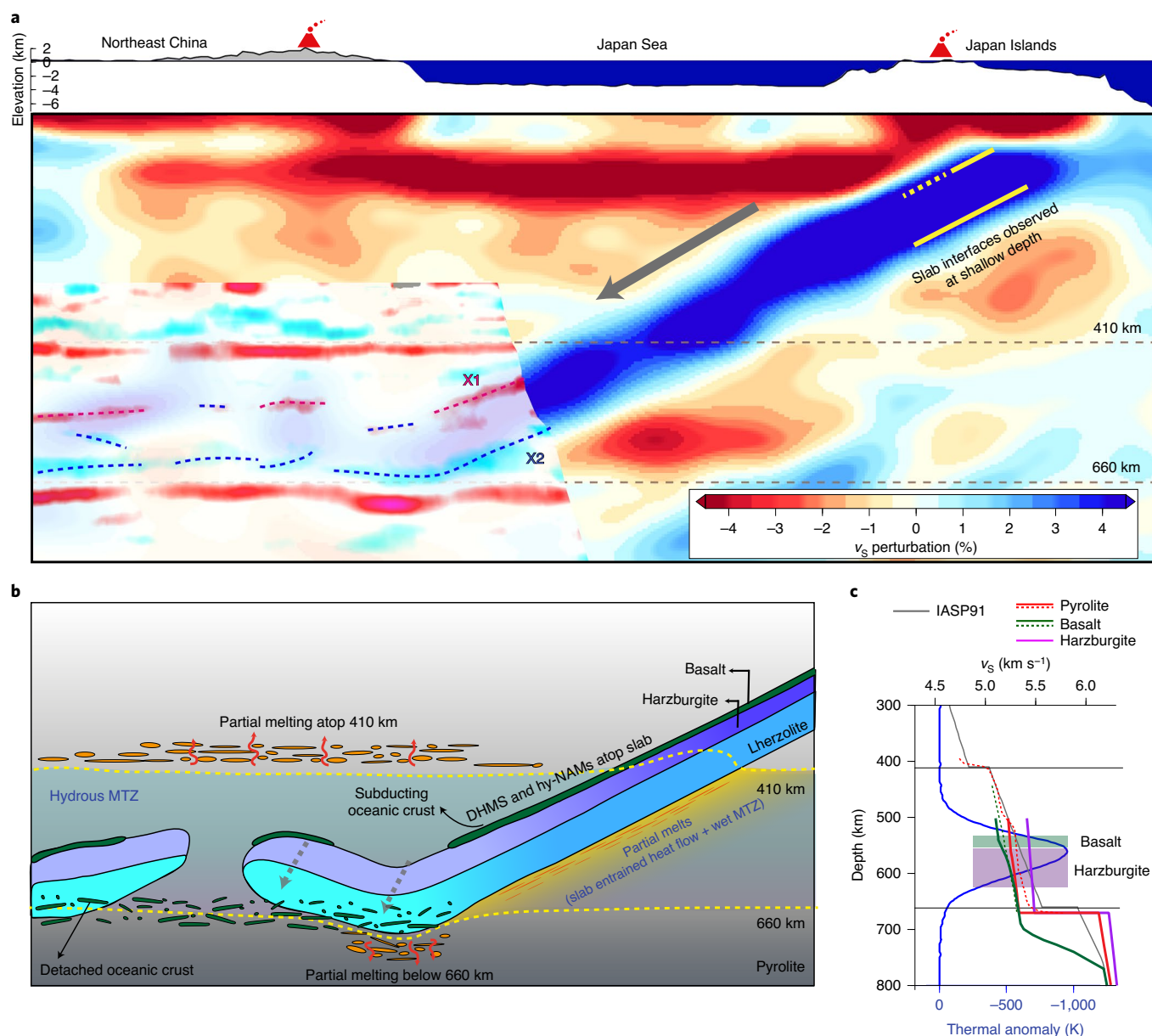


Fig. 4 | Observations show that the slab interfaces can persist to MTZ depths. a, Our seismic observations, slab interfaces observed at shallow depth⁵ and seismic tomographic image of v_s (ref.⁴), showing a general picture of seismic observations in the region. **b**, A conceptual cartoon summarizing our interpretations and earlier observations of the MTZ. The slab interfaces can be seismologically discerned mainly by the existence of compositional heterogeneities (petrological structure and hydration). **c**, Shear-velocity profiles of typical mantle rocks in the MTZ, where the solid lines are from Gréaux et al.³² and the dashed lines are from Irifune et al.²⁹ and Kono et al.³⁸. For comparison, the 1D v_s model from IASP91⁴⁹ is shown as a solid grey line. Blue lines show the slab thermal anomaly from geodynamic modelling. DHMSs, dense hydrous magnesium silicates; hy-NAMs, Hydrated nominally anhydrous minerals.

even if the excessive heat beneath the slab is absent, provided the MTZ is sufficiently wet, partial melting can still occur due to the reduced solidus⁴⁸.

In the northwest Pacific subduction zone, the boundaries between high-velocity slabs and the surrounding mantle are observed as sharp seismic velocity discontinuities, extending down to 200 km depth^{5,6}. The boundaries can be seismologically detected mainly owing to the presence of fluids or melting at the slab boundaries^{5,7,39}. In this study, we observed well-constrained parallel seismic velocity discontinuities at the top and bottom of the subducting Pacific slab at MTZ depths. Although the mechanisms that enhance seismic contrasts across slab interfaces in the MTZ are not known, slab lithological structures and the existence of partial melt and/or concentrated volatiles near the slab may help

to reveal the origin of these sharp seismic interfaces. A better understanding of these interesting observations requires new numerical simulations to understand slab–mantle interactions, high-pressure/high-temperature experiments to better constrain the elastic properties of mantle rocks and more seismic observations to enhance the resolution of these deep reflectors.

Online content

Any methods, additional references, Nature Research reporting summaries, source data, extended data, supplementary information, acknowledgements, peer review information; details of author contributions and competing interests; and statements of data and code availability are available at <https://doi.org/10.1038/s41561-020-00653-5>.

Received: 22 October 2018; Accepted: 30 September 2020;
Published online: 09 November 2020

References

- Hacker, B. R., Abers, G. A. & Peacock, S. M. Subduction factory 1. Theoretical mineralogy, densities, seismic wave speeds, and H₂O contents. *J. Geophys. Res. Solid Earth* **108**, 133–137 (2003).
- Fukao, Y. & Obayashi, M. Subducted slabs stagnant above, penetrating through, and trapped below the 660 km discontinuity. *J. Geophys. Res. Solid Earth* **118**, 5920–5938 (2013).
- Huang, J. L. & Zhao, D. P. High-resolution mantle tomography of China and surrounding regions. *J. Geophys. Res. Solid Earth* **111**, B09305 (2006).
- Tao, K., Grand, S. P. & Niu, F. Seismic structure of the upper mantle beneath eastern Asia from full waveform seismic tomography. *Geochem. Geophys. Geosyst.* **19**, 2732–2763 (2018).
- Kawakatsu, H. et al. Seismic evidence for sharp lithosphere-asthenosphere boundaries of oceanic plates. *Science* **324**, 499–502 (2009).
- Kawakatsu, H. & Watada, S. Seismic evidence for deep-water transportation in the mantle. *Science* **316**, 1468–1471 (2007).
- Stern, T. A. et al. A seismic reflection image for the base of a tectonic plate. *Nature* **518**, 85–88 (2015).
- Tonegawa, T. et al. Water flow to the mantle transition zone inferred from a receiver function image of the Pacific slab. *Earth Planet. Sci. Lett.* **274**, 346–354 (2008).
- Iwamori, H. Transportation of H₂O beneath the Japan arcs and its implications for global water circulation. *Chem. Geol.* **239**, 182–198 (2007).
- Yang, J. & Faccenda, M. Intraplate volcanism originating from upwelling hydrous mantle transition zone. *Nature* **579**, 88–91 (2020).
- Ohtani, E. Water in the mantle. *Elements* **1**, 25–30 (2005).
- Kawakatsu, H. & Utada, H. Seismic and electrical signatures of the lithosphere-asthenosphere system of the normal oceanic mantle. *Annu. Rev. Earth Planet. Sci.* **45**, 139–167 (2017).
- Langston, C. A. Structure under Mount Rainier, Washington, inferred from teleseismic body waves. *J. Geophys. Res.* **84**, 4749–4762 (1979).
- Zhu, L. P. Crustal structure across the San Andreas Fault, southern California from teleseismic converted waves. *Earth Planet. Sci. Lett.* **179**, 183–190 (2000).
- Bercovici, D. & Karato, S. Whole-mantle convection and the transition-zone water filter. *Nature* **425**, 39–44 (2003).
- Engdahl, E. R. et al. ISC-EHB 1964–2016, an improved data set for studies of Earth structure and global seismicity. *Earth Space Sci.* **7**, e2019EA000897 (2020).
- Tauzin, B., Debayle, E. & Wittlinger, G. Seismic evidence for a global low-velocity layer within the Earth's upper mantle. *Nat. Geosci.* **3**, 718–721 (2010).
- van der Meijde, M., Marone, F., Giardini, D. & van der Lee, S. Seismic evidence for water deep in Earth's upper mantle. *Science* **300**, 1556–1558 (2003).
- Bostock, M. G. Seismic waves converted from velocity gradient anomalies in the Earth's upper mantle. *Geophys. J. Int.* **138**, 747–756 (1999).
- Shearer, P. M. Seismic imaging of upper-mantle structure with new evidence for a 520-km discontinuity. *Nature* **344**, 121–126 (1990).
- Deuss, A. & Woodhouse, J. Seismic observations of splitting of the mid-transition zone discontinuity in Earth's mantle. *Science* **294**, 354–357 (2001).
- Saikia, A., Frost, D. J. & Rubie, D. C. Splitting of the 520-kilometer seismic discontinuity and chemical heterogeneity in the mantle. *Science* **319**, 1515–1518 (2008).
- Sinogeikin, S. V., Bass, J. D. & Katsura, T. Single-crystal elasticity of ringwoodite to high pressures and high temperatures: implications for 520 km seismic discontinuity. *Phys. Earth Planet. Inter.* **136**, 41–66 (2003).
- Valdez, M. N., Wu, Z. Q., Yu, Y. G., Revenaugh, J. & Wentzcovitch, R. M. Thermoelastic properties of ringwoodite (Fe_xMg_{1-x})₂SiO₄: its relationship to the 520 km seismic discontinuity. *Earth Planet. Sci. Lett.* **351**, 115–122 (2012).
- Tauzin, B., Kim, S. & Afonso, J. C. Multiple phase changes in the mantle transition zone beneath northeast Asia: constraints from teleseismic reflected and converted body waves. *J. Geophys. Res. Solid Earth* **123**, 6636–6657 (2018).
- Xu, W. B., Lithgow-Bertelloni, C., Stixrude, L. & Ritsema, J. The effect of bulk composition and temperature on mantle seismic structure. *Earth Planet. Sci. Lett.* **275**, 70–79 (2008).
- Tauzin, B. & Ricard, Y. Seismically deduced thermodynamics phase diagrams for the mantle transition zone. *Earth Planet. Sci. Lett.* **401**, 337–346 (2014).
- Yang, J. et al. Slab-triggered wet upwellings produce large volumes of melt: insights into the destruction of the North China Craton. *Tectonophysics* **746**, 266–279 (2018).
- Irifune, T. et al. Sound velocities of majorite garnet and the composition of the mantle transition region. *Nature* **451**, 814–817 (2008).
- Li, D., Helmberger, D., Clayton, R. W. & Sun, D. Global synthetic seismograms using a 2-D finite-difference method. *Geophys. J. Int.* **197**, 1166–1183 (2014).
- Ringwood, A. E. & Irifune, T. Nature of the 650-km seismic discontinuity: implications for mantle dynamics and differentiation. *Nature* **331**, 131–136 (1988).
- Gréaux, S. et al. Sound velocity of CaSiO₃ perovskite suggests the presence of basaltic crust in the Earth's lower mantle. *Nature* **565**, 218–221 (2019).
- Shen, Y. & Blum, J. Seismic evidence for accumulated oceanic crust above the 660-km discontinuity beneath southern Africa. *Geophys. Res. Lett.* **30**, 1925 (2003).
- Eagar, K. C., Fouch, M. J. & James, D. E. Receiver function imaging of upper mantle complexity beneath the Pacific Northwest, United States. *Earth Planet. Sci. Lett.* **297**, 141–153 (2010).
- Tauzin, B., Kim, S. & Kennett, B. L. N. Pervasive seismic low-velocity zones within stagnant plates in the mantle transition zone: thermal or compositional origin? *Earth Planet. Sci. Lett.* **477**, 1–13 (2017).
- Shen, X., Yuan, X. & Li, X. A ubiquitous low-velocity layer at the base of the mantle transition zone. *Geophys. Res. Lett.* **41**, 836–842 (2014).
- Ganguly, J., Freed, A. M. & Saxena, S. K. Density profiles of oceanic slabs and surrounding mantle: integrated thermodynamic and thermal modeling, and implications for the fate of slabs at the 660km discontinuity. *Phys. Earth Planet. Inter.* **172**, 257–267 (2009).
- Kono, Y., Irifune, T., Ohfuji, H., Higo, Y. & Funakoshi, K. Sound velocities of MORB and absence of a basaltic layer in the mantle transition region. *Geophys. Res. Lett.* **39**, L24306 (2012).
- Hawley, W. B., Allen, R. M. & Richards, M. A. Tomography reveals buoyant asthenosphere accumulating beneath the Juan de Fuca plate. *Science* **353**, 1406–1408 (2016).
- Phipps Morgan, J., Hasenclever, J., Hort, M., Rüpke, L. & Parmentier, E. M. On subducting slab entrainment of buoyant asthenosphere. *Terra Nova* **19**, 167–173 (2007).
- Tang, Y. et al. Changbaishan volcanism in northeast China linked to subduction-induced mantle upwelling. *Nat. Geosci.* **7**, 470–475 (2014).
- Liu, L. & Zhou, Q. Deep recycling of oceanic asthenosphere material during subduction. *Geophys. Res. Lett.* **42**, 2204–2211 (2015).
- Obayashi, M., Sugioka, H., Yoshimitsu, J. & Fukao, Y. High temperature anomalies oceanward of subducting slabs at the 410-km discontinuity. *Earth Planet. Sci. Lett.* **243**, 149–158 (2006).
- Kelbert, A., Schultz, A. & Egbert, G. Global electromagnetic induction constraints on transition-zone water content variations. *Nature* **460**, 1003–1006 (2009).
- Li, J., Wang, X., Wang, X. J. & Yuen, D. A. P and SH velocity structure in the upper mantle beneath Northeast China: evidence for a stagnant slab in hydrous mantle transition zone. *Earth Planet. Sci. Lett.* **367**, 71–81 (2013).
- Fei, H. & Katsura, T. High water solubility of ringwoodite at mantle transition zone temperature. *Earth Planet. Sci. Lett.* <https://doi.org/10.1016/j.epsl.2019.115987> (2019).
- Hirose, K. Phase transitions in pyrolitic mantle around 670-km depth: implications for upwelling of plumes from the lower mantle. *J. Geophys. Res. Solid Earth* **107**, 2078 (2002).
- Litasov, K. D. & Ohtani, E. in *Advances in High-Pressure Mineralogy* 115–156 (GSA, 2007).
- Kennett, B. L. N. & Engdahl, E. R. Traveltimes for global earthquake location and phase identification. *Geophys. J. Int.* **105**, 429–465 (1991).
- Dziewonski, A. M. & Anderson, D. L. Preliminary reference Earth model. *Phys. Earth Planet. Inter.* **25**, 297–356 (1981).

Publisher's note Springer Nature remains neutral with regard to jurisdictional claims in published maps and institutional affiliations.

© The Author(s), under exclusive licence to Springer Nature Limited 2020

Methods

RF data processing. Seismic data for this study were collected from 313 regional broadband seismic stations in northeast China (Extended Data Fig. 1a). These stations belong to three seismic arrays: (1) 58 temporary stations from the Northeast China Seismic Array to Investigate Deep Subduction (NECsaid) between September 2009 and December 2014, (2) 127 temporary stations from the Northeast China Extended Seismic Array (NECESSArray)⁵¹ between September 2009 and August 2011 and (3) 128 permanent stations from the China Earthquake Administration array (CEA)⁵² between July 2007 and December 2014. The high density and high quality of the seismic stations in northeast China provide excellent opportunities to finely image the upper mantle structures.

We used the P-to-S RF technique¹³, which is particularly powerful for capturing the velocity discontinuities beneath the seismic station, to study the upper mantle structures beneath northeast China. We analysed waveform data from teleseismic events with magnitudes larger than 5.2 and epicentral distances ranging from 30 to 90° (Extended Data Fig. 1b). Raw seismograms were windowed between 20 s before and 100 s after the first P-wave arrival, and then the three-component seismograms were rotated to the radial, transverse and vertical components. For some of the seismic stations that have reported seismic sensor misorientation^{53,54}, we corrected the sensor misorientation before rotation. The three-component seismograms were then filtered with a 50-s to 2-Hz zero-phase filter to eliminate both long-period and high-frequency noise. We then calculated the signal-to-noise ratio (SNR) of each waveform and selected only those that have $\text{SNR}_{\text{BHZ}} > 3$ for further analysis. Here BHZ indicates the vertical component recording. We obtained the RF by deconvolving the vertical component from the radial component using a time-domain iterative deconvolution technique with a Gaussian low-pass filter⁵⁵. Various values of the Gaussian parameter $a = 0.5, 0.75, 1.0$ and 1.5 (roughly corresponding to corner frequencies of 0.25, 0.35, 0.5 and 0.7 Hz) were used to conduct the frequency-dependent RF analysis. The radial RF was then normalized by the maximum amplitude of the vertical RF, which was obtained by self-deconvolution, to obtain the true amplitudes⁵⁶. After the deconvolution, we discarded RF waveforms that showed large amplitude coda after the first P-wave arrival (greater than 20% of the P waves in the time window 20–80 s). Careful visual inspection was further conducted to remove bad traces with low coherence. A total of 67,344 high-quality RFs were selected from 1,858 events for further imaging. Most of the RFs were derived from earthquakes located to the southeast of the array (Extended Data Fig. 1c). Supplementary Figs. 1 and 2 show the distribution of the P-to-S conversion points at 410 and 660 km depths. The profiles shown in Fig. 2 have been densely sampled by the Ps conversion points at MTZ depths.

CCP stacking. We used the CCP stacking technique¹⁴ to image the lateral variations of the upper mantle structures. For an assumed conversion depth, d , the delay time of P-to-s conversions and the corresponding geographic locations were back-projected along the ray path determined by one-dimensional ray tracing using the IASP91 model⁴⁹. To account for the lateral 3D velocity structure effect, travel time corrections were made by employing the recent high-resolution regional full-waveform 3D FWEA18 tomography models from Tao et al.⁴.

We adopted a moving window of 5 km in the horizontal direction and then used rectangular bins with 50 km (half bin size) along the direction of the profile and ~50 km orthogonal (half bin size) to the profile to construct the stacking image. The amplitude in each bin was obtained by averaging all the RFs with conversion points within each bin. To ensure reliability, we only selected bins with more than 100 RFs for final imaging, although most of the bins had more than 500 RFs (Supplementary Fig. 1). The high-density dataset helped us to finely image the MTZ structures. In addition to profiles A and B shown in Fig. 2, we displayed 10 profiles along different latitudes to demonstrate that phases X1 and X2 are ubiquitous across the study area (Extended Data Figs. 2 and 3).

In this study, we also conduct detailed analysis to demonstrate that phases X1 and X2 are well resolved beyond the noise level (Supplementary Section 3), and are not caused by the side-lobes in data processing (Supplementary Section 4) nor multiple reverberations from shallow structures (Supplementary Section 5). The comparison of our CCP stacking images and the tomography studies suggests that there might be a relation between the geometry of the plate and these X1 and X2 convertors (Extended Data Fig. 2 and Fig. 3). We picked the signals related to phases X1 and X2, and conducted a systemic comparison of phases X1 and X2 and the slab-related fast-velocity anomaly contours (v_s of 1%, 2% and 3%) in tomographic studies⁴ (Supplementary Fig. 3). The correlation analysis suggests that the existence of phases X1/X2 is best correlated with a velocity contour of 1.0% with a correlation coefficient (CC) of 0.5 (Extended Data Fig. 4), whereas the depth of phases X1/X2 is best correlated with the velocity contour of 3.0% with a CC of 0.3 (Extended Data Fig. 4). The discrepancies between phases X1/X2 and the slab geometries could partially be due to (1) phases X1/X2 occurring within a certain thickness and (2) the complexities and uncertainties in both the reflectivity structure and tomography studies. In addition, we want to point out that phases X1 and X2, located in the western of longitude 130° E, tend to be affected by the existence of the Songliao basin³⁵ (Supplementary Section 5). Thus, we divided our study region into the flattened section and the dipping section by using the distance along the profiles (Extended Data Fig. 4). By only focusing on the dipping

section, the CC between phases X1 and X2 and the slab contours are substantially improved, reaching a CC of 0.65. The high CC suggests that phases X1 and X2 are consistent with the boundaries between the subducting Pacific slab and the surrounding mantle.

Multi-frequency RF waveform modelling. The arrival time and amplitude of P-to-S converted phases on the RF waveform can be used to constrain the seismic properties of the discontinuity, such as the depth, velocity contrast and sharpness. For a seismic velocity discontinuity defined with a certain thickness (a gradual velocity transition), the measured amplitude of the RF waveform varies with frequency¹⁸. In this study, we use multi-frequency RF waveform modelling to constrain the seismic velocity properties corresponding to phases X1 and X2.

To obtain a more intuitive insight into the frequency-dependent amplitudes of RF waveforms, we first conducted a series of synthetic tests. The synthetic RFs for a given isotropic layered model were obtained by numerically deconvolving the synthetic radial component from the vertical component through a time-domain iterative deconvolution. We use the 1D IASP91 model⁴⁹ as our reference model and employed a variety of velocity perturbations around 500–600 km depth to mimic the effect of a high-velocity subducting slab (Extended Data Fig. 5). We used the maximum shear-velocity contrast across the discontinuity (dv_s) and the thickness of the discontinuity (ΔH) to describe the velocity properties of the discontinuity (Extended Data Fig. 5a), where $\Delta H = 0$ km corresponds to a sharp discontinuity. For a given velocity model, we generated a group of synthetic RFs with different ray parameters to represent the RFs at different epicentral distances. Then, the RFs were move-out corrected, stacked and converted to depth to represent the theoretical RF for a given velocity model (Extended Data Fig. 5b–d). In our deconvolution procedure, we applied a Gaussian low-pass filter of $a = 0.5$ – 2.0 (corresponding to a corner frequency of 0.24–1.0 Hz) to study the frequency-dependent amplitude of the RF waveforms. In our study, we used a constant high-pass cutoff of 0.02 Hz, as our aim was to explore how sharp phases X1 and X2 could be. A series of narrow-frequency band filters would be helpful to provide a full understanding of the sharpness of the discontinuities, but remain a matter for future investigations.

The amplitude of the P-to-S phase increases with increasing velocity contrast, as the transmission coefficients become larger (Extended Data Fig. 5b). For a constant Gaussian filter, the P-to-S phase will become broader in shape and smaller in amplitude as the transition thickness increases (Extended Data Fig. 5c). When the transition thickness is larger, the amplitude of the P-to-S phase will change more dramatically with the frequency, as the wavelength of the incoming wave has a finite width, and therefore averages over a certain depth range (Extended Data Fig. 5d). Extended Data Fig. 6 shows a diagram of the variation of the amplitude of the P-to-S phase as a function of transition thickness, velocity perturbation and frequency. The frequency-dependent amplitude of the P-to-S phase in the real data is given in Extended Data Fig. 6g,h, with uncertainties estimated by a bootstrapping method⁵⁷. The large amplitudes of the 410 km (d410) and 660 km (d660) discontinuities, and phases X1 and X2 at low frequency ($a = 0.5$) suggest that these discontinuities correspond to large velocity jumps. Both for the d410, d660 and the positive (X1) and negative (X2) phases, the amplitude decreases with the increasing frequency, indicating that the discontinuity is smoother, rather than sharper. With this information, we used forward modelling to obtain the simple and best-fitting model by fitting the multi-frequency RF waveforms (Fig. 2). The velocity structures are well constrained, both in terms of the sharpness and velocity jump, as we could fit the multi-frequency RF waveforms simultaneously (Extended Data Fig. 7a,b). We should note here that the RF waveforms are more sensitive to the velocity change in depth than to the absolute velocity value (Extended Data Fig. 7c).

Data availability

Seismic data from CSN were provided by the Data Management Center of China National Seismic Network at Institute of Geophysics, China Earthquake Administration (<https://doi.org/10.11998/SeisDmc/SN>, <http://www.seisdmc.ac.cn>), registration is required to download the data, in Chinese). The NECESSArray data were downloaded through the Incorporated Research Institutions for Seismology (https://doi.org/10.7914/SN/YP_2009). Waveforms of the NECsaids data are deposited in the Seismic Array Laboratory, Institute of Geology and Geophysics, Chinese Academy of Sciences (<https://doi.org/10.12129/IGGSL.Data.Observation>, <http://www.seislab.cn>) and can be downloaded via <ftp://159.226.119.161/data/NECsaid/RF2020>. The Seismic Array Laboratory will make the NECsaids Array data publicly available from October 2021 (three years after the completion of the NECsaids project). In addition, the raw multi-frequency (with Gaussian low-pass filters of 0.5, 0.75, 1.0 or 1.5) receiver function waveform data (2.7Gb) obtained in this study can be downloaded either from <https://doi.org/10.12197/2020GA012> (World Data System for Geophysics; <http://www.geophys.ac.cn>) or from <ftp://159.226.119.161/data/NECsaid/RF2020>.

Code availability

The RF CCP stacking code was downloaded from <http://www.eas.slu.edu/People/LZhu/home.html>. The other codes used in this paper are available upon request from the corresponding authors.

References

51. Ni, J. *Collaborative Research: Northeast China Extended Seismic Array: Deep Subduction, Mantle Dynamics and Lithospheric Evolution Beneath Northeast China* (International Federation of Digital Seismograph Networks, 2009); https://doi.org/10.7914/SN/YP_2009
52. *Waveform Data of China National Seismic Network* (in Chinese) (Institute of Geophysics, Data Management Centre of China National Seismic Network, 2007); <https://doi.org/10.11998/SeisDmc/SN>
53. Niu, F. & Li, J. Component azimuths of the CEArray stations estimated from P-wave particle motion. *Earthq. Sci.* **24**, 3–13 (2011).
54. Wang, X., Chen, Q. F., Li, J. & Wei, S. J. Seismic sensor misorientation measurement using P-wave particle motion: an application to the NECsaids array. *Seismol. Res. Lett.* **84**, 901–911 (2016).
55. Ligorria, J. P. & Ammon, C. J. Iterative deconvolution and receiver-function estimation. *Bull. Seismol. Soc. Am.* **89**, 1395–1400 (1999).
56. Ammon, C. J. The isolation of receiver effects from teleseismic P waveforms. *Bull. Seismol. Soc. Am.* **81**, 2504–2510 (1991).
57. Efron, B. & Tibshirani, R. Statistical data analysis in the computer age. *Science* **253**, 390–395 (1991).
58. Schulze, K. et al. Seismically invisible water in Earth's transition zone? *Earth Planet. Sci. Lett.* **498**, 9–16 (2018).
59. Buchen, J. et al. High-pressure single-crystal elasticity of wadsleyite and the seismic signature of water in the shallow transition zone. *Earth Planet. Sci. Lett.* **498**, 77–87 (2018).
60. Li, C. & van der Hilst, R. D. Structure of the upper mantle and transition zone beneath Southeast Asia from traveltimes tomography. *J. Geophys. Res. Solid Earth* **115**, B07308 (2010).

Acknowledgements

We thank L. Chen, H. Kawakatsu, T.-R. A. Song, S. P. Grand, J. Yang and J. Hu for numerous discussions during this work. We thank all the people who installed and service the NECsaids array. We also thank V. Lambert and P. Adamek for linguistic suggestions. This study was supported by the Strategic Priority Research Program (B) of the Chinese Academy of Sciences (grant number XDB18000000) and the National Natural Science Foundation of China (grant numbers 91958209, 41974057, 41130316 and 41630209). J.B. was supported by the National Science Foundation's Collaborative Study of Earth's Deep Interior (EAR-1161046 and EAR-2009935).

Author contributions

X.W. and Q.-F.C. designed the research. X.W. conducted the seismic analysis. X.W., Q.-F.C., F.N., J.B. and L.L. contributed to the interpretation of seismic observations. X.W. wrote the manuscript, and all co-authors discussed the results and commented on the manuscript.

Competing interests

The authors declare no competing interests.

Additional information

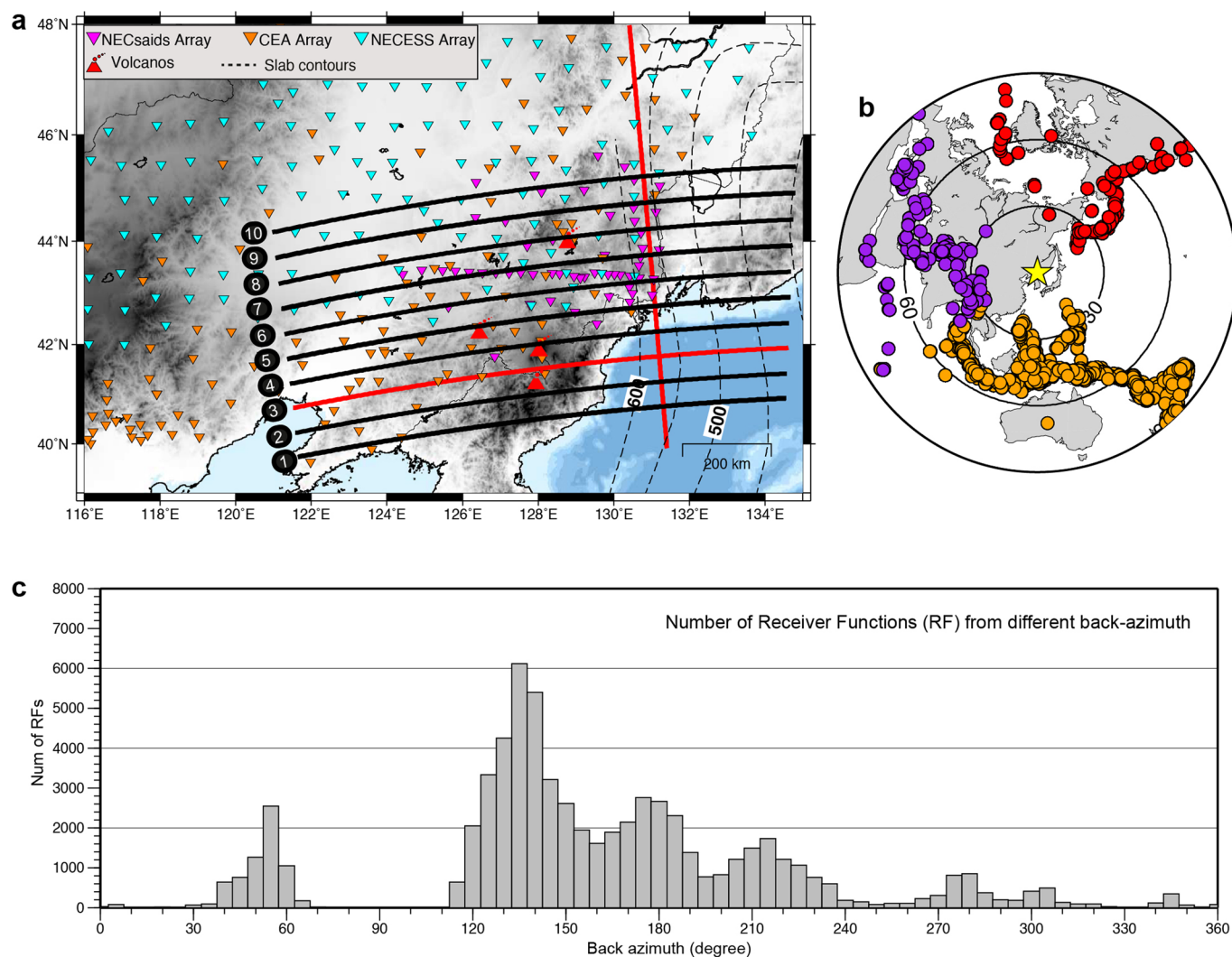
Extended data is available for this paper at <https://doi.org/10.1038/s41561-020-00653-5>.

Supplementary information is available for this paper at <https://doi.org/10.1038/s41561-020-00653-5>.

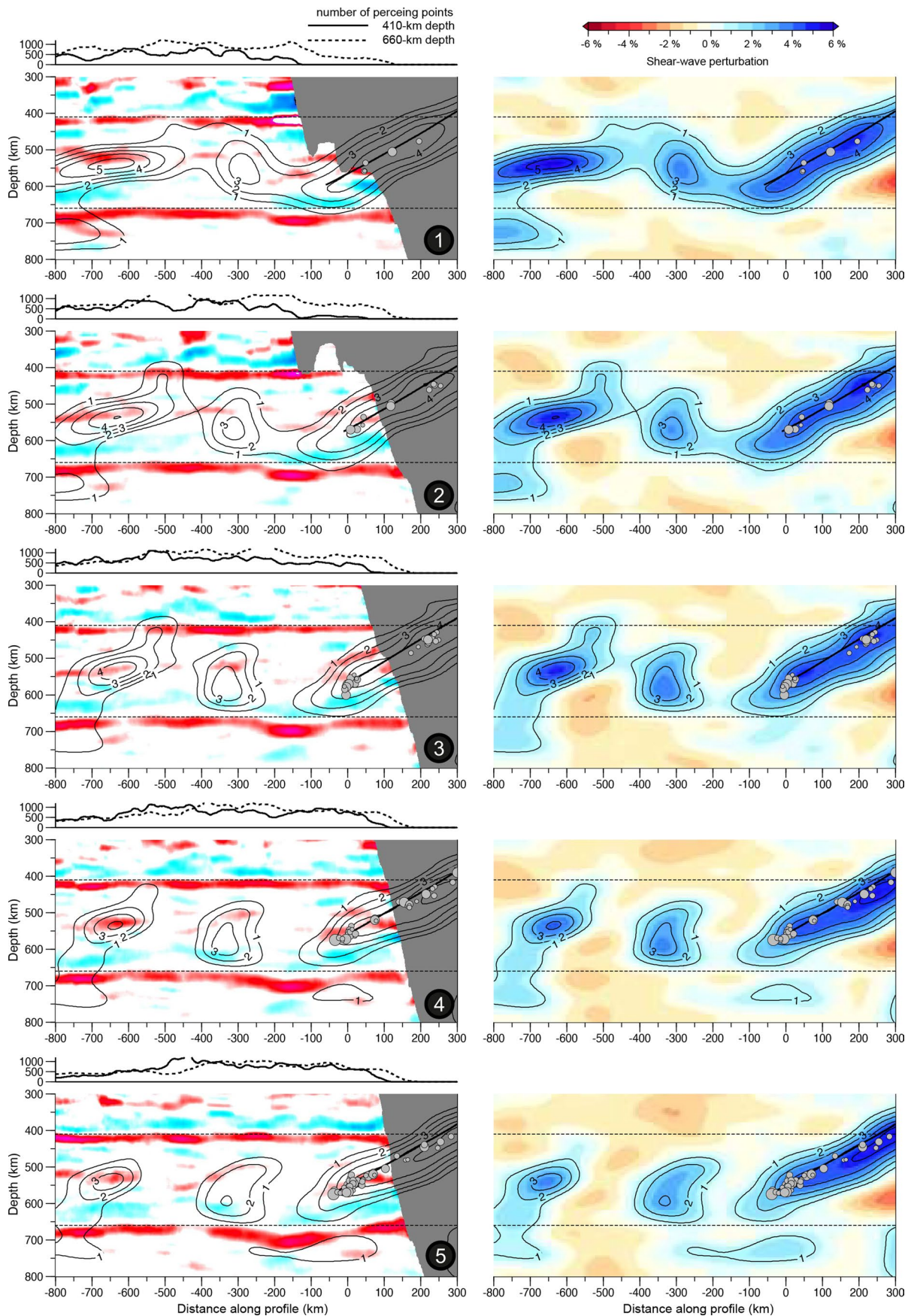
Correspondence and requests for materials should be addressed to Q.-F.C. or F.N.

Peer review information Primary Handling Editors: Stefan Lachowycz; Melissa Plail.

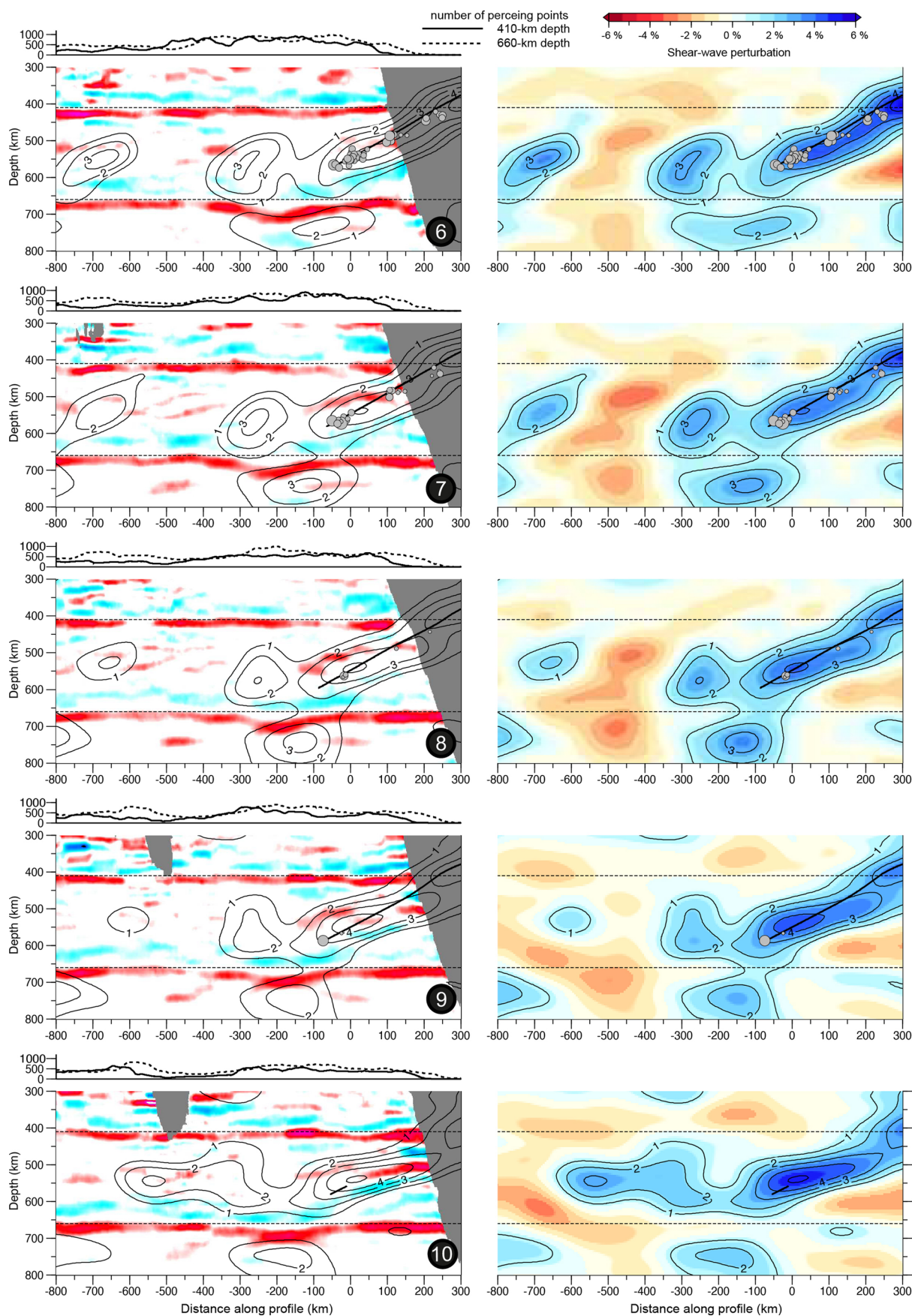
Reprints and permissions information is available at www.nature.com/reprints.



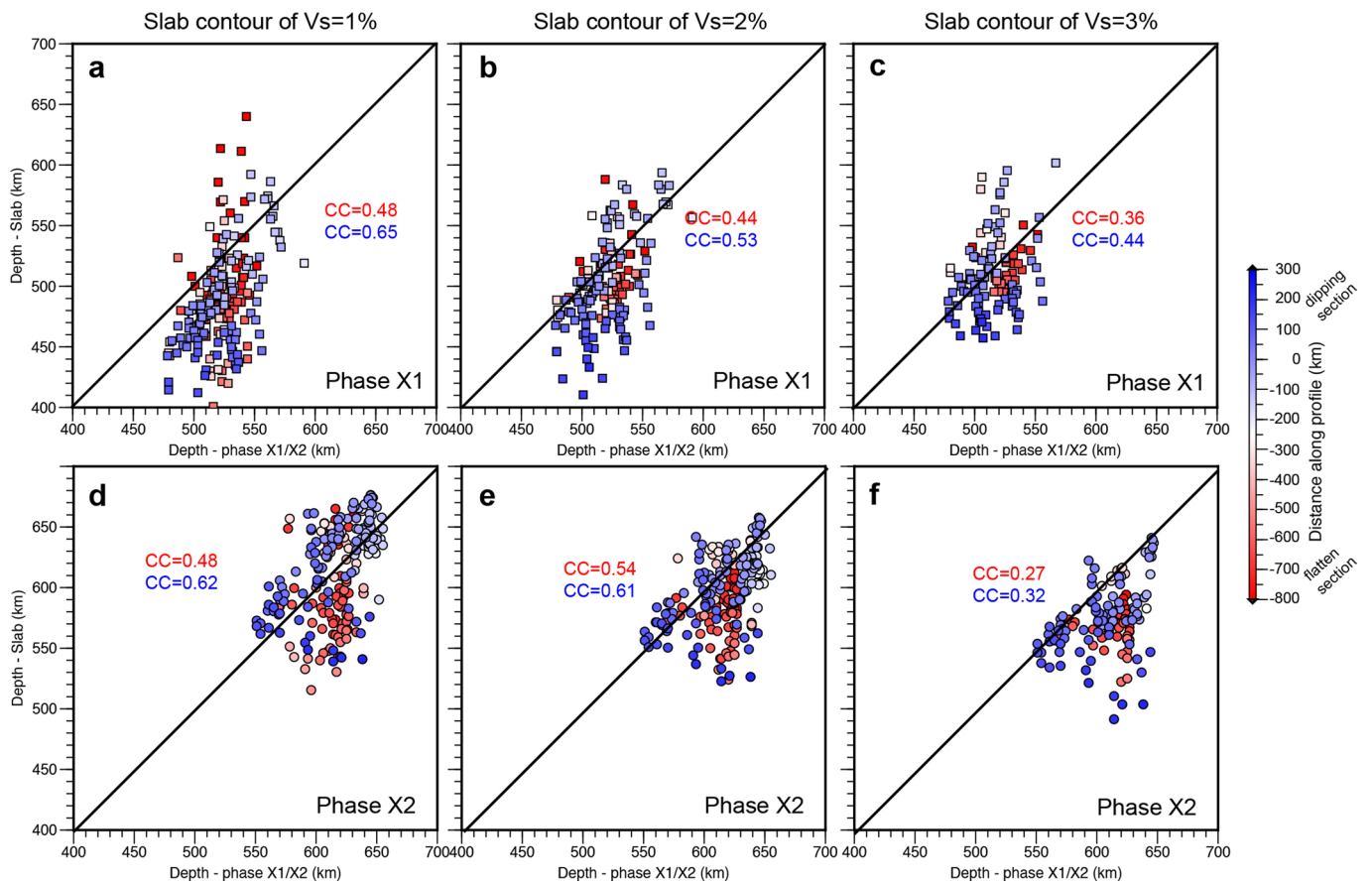
Extended Data Fig. 1 | Seismic stations and earthquakes used in this study. **a**, Study region and locations of broadband seismic stations (triangles) used in this study. The thick red lines give the location of the profiles shown in Fig. 2 in the main text. The black lines (numbered from 1 to 10) give the location of the profiles shown in Extended Data Figs. 2 and 3, to demonstrate the non-uniqueness of the phases X1 and X2. Black dashed curves show the Wadati-Benioff zone obtained from the distribution of intermediate/deep earthquakes. The red symbols indicate the Cenozoic active volcanoes in this region. **b**, Spatial distribution of earthquakes used in receiver function study, colored by their back azimuth. **c**, Histogram shows the number of receiver functions from different back azimuth.



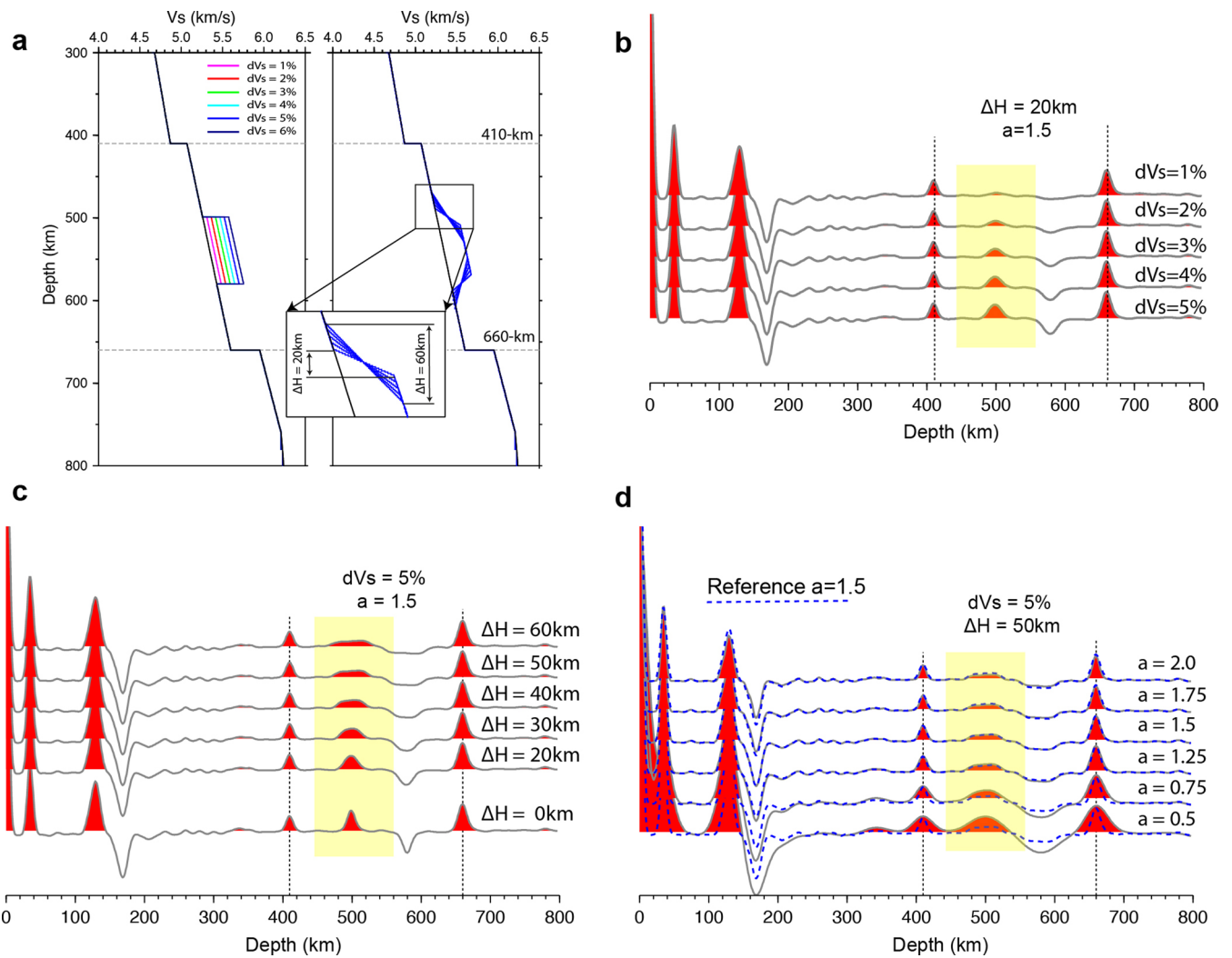
Extended Data Fig. 2 | Comparison of CCP stacking images and the tomography studies. Receiver function common conversion point stacking images along the five profiles (1-5) shown in Extended Data Fig. 1. For comparison, the corresponding full-waveform tomographic images from Tao et al.⁴ are shown. The subducting Pacific slab is highlighted by positive velocity anomaly contours.



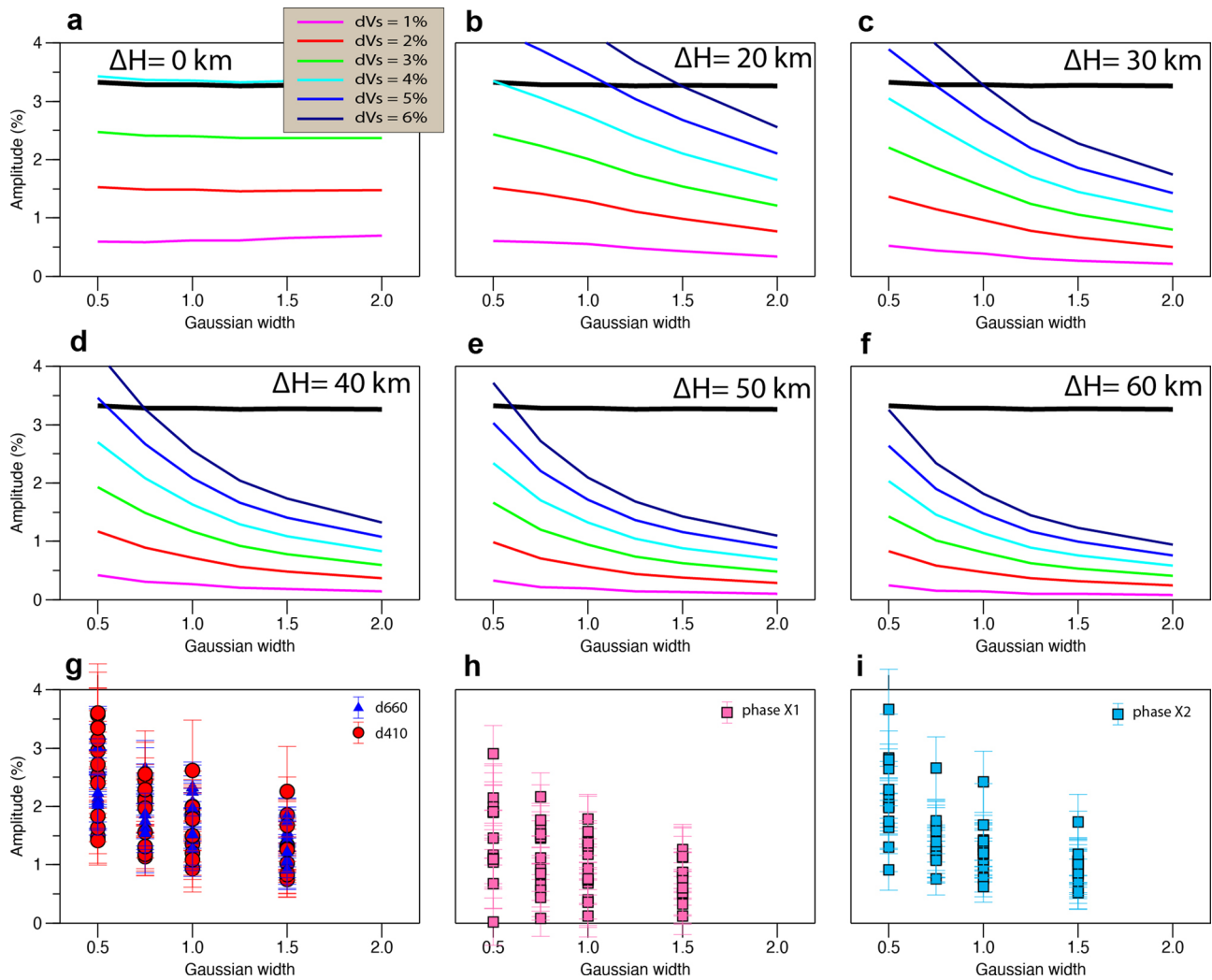
Extended Data Fig. 3 | Comparison of CCP stacking images and the tomography studies. Same as Extended Data Fig. 2, but for five profiles (6-10) shown in Extended Data Fig. 1.



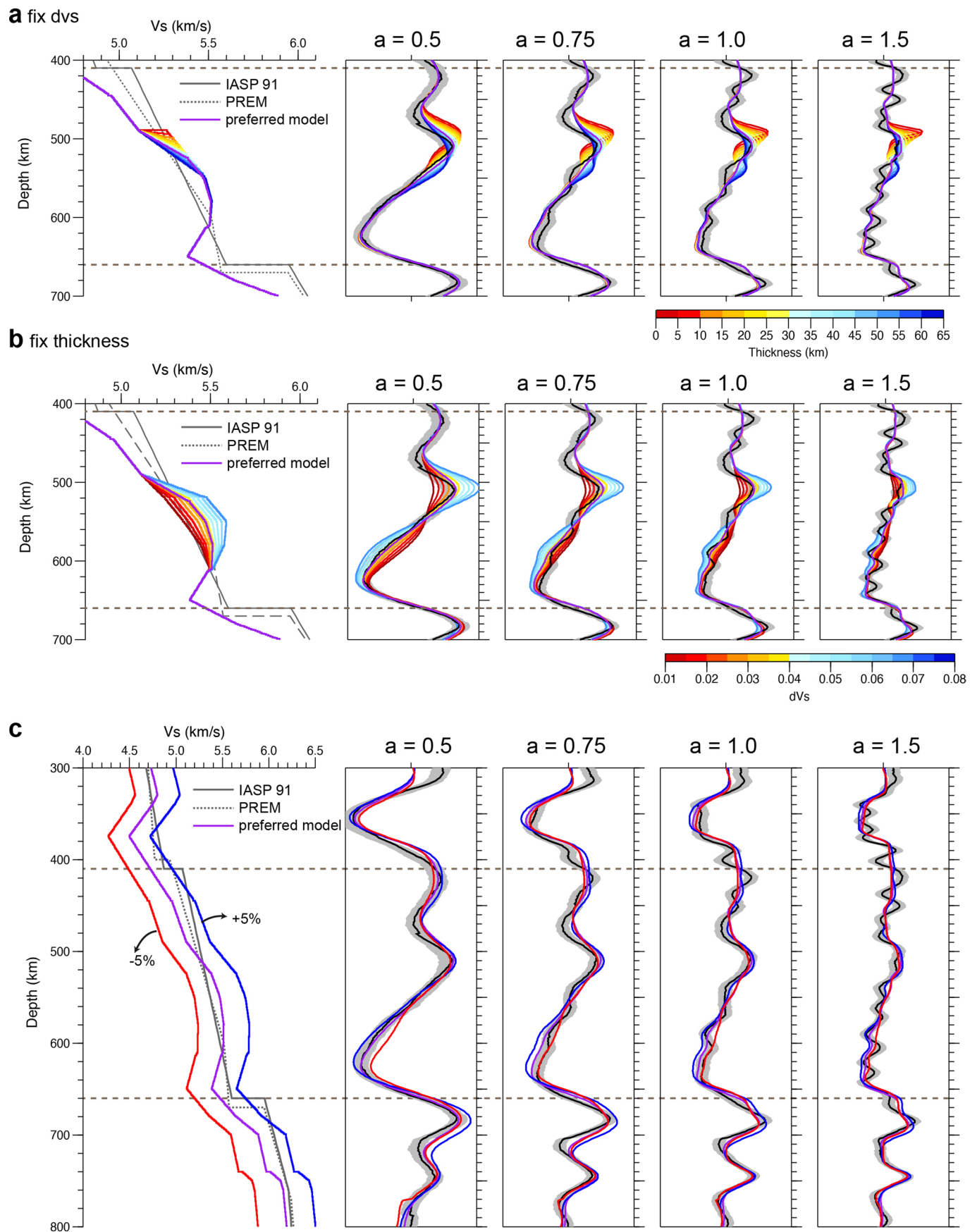
Extended Data Fig. 4 | Cross-correlation analyze of the phases X1 and X2 and the slab-related fast-velocity anomaly contours in tomographic studies. We use the Pearson correlation coefficient (CC) to qualify the correlation between phases X1 **a-c**, and X2 **d-f**, and the velocity contours. Our study suggests that the existence of the phases X1/X2 is best correlated with velocity contour of 1%, while the depth of the phases X1/X2 is best correlated with the velocity of 3%.



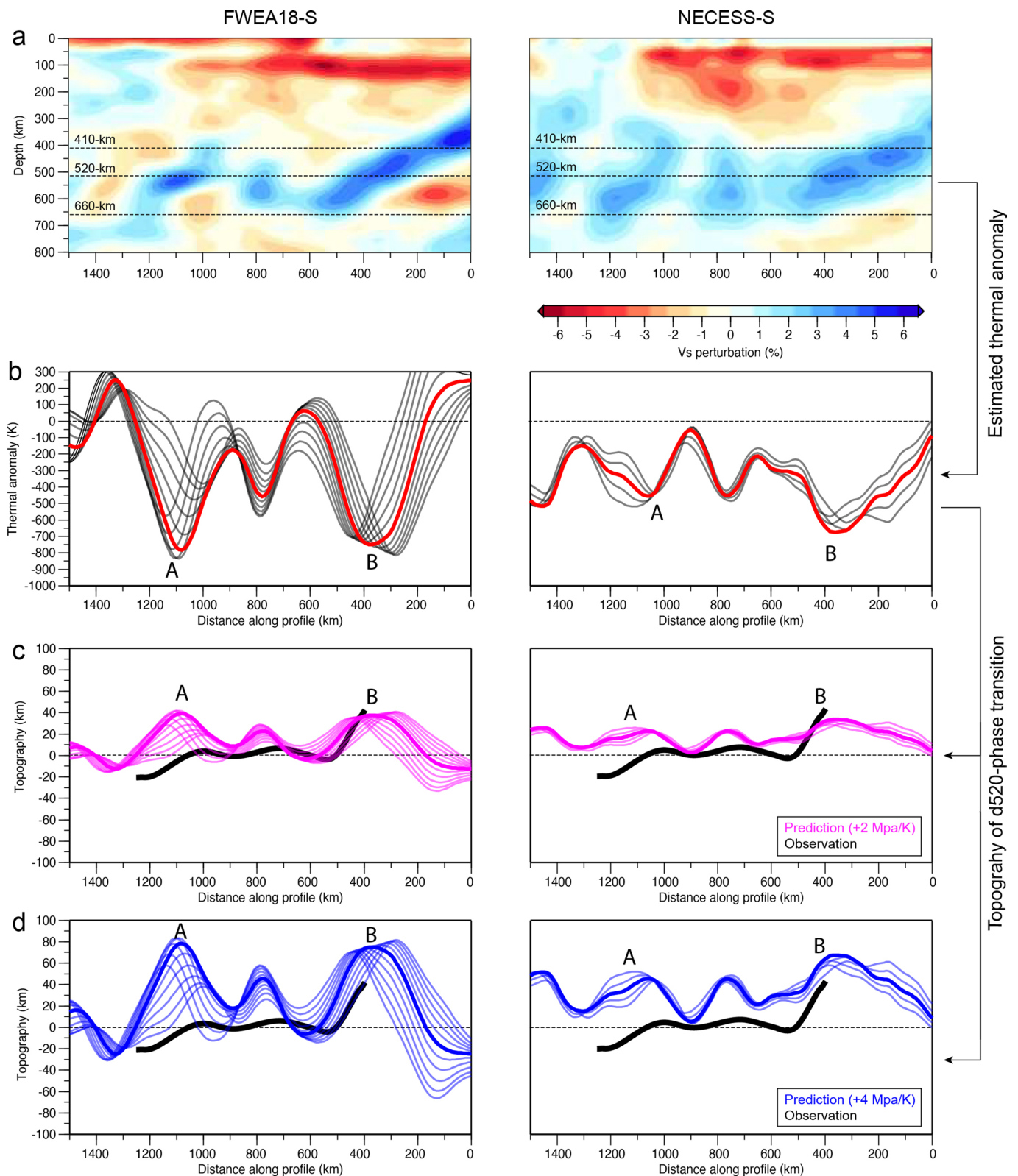
Extended Data Fig. 5 | Multi-frequency receiver function waveform modeling. **a**, The 1D velocity model set up in Receiver Function synthetic tests. **b**, Sensitivity to the velocity contrast. **c**, Sensitivity to the transition thickness. **d**, Sensitivity to the Gaussian filter parameter (frequency).



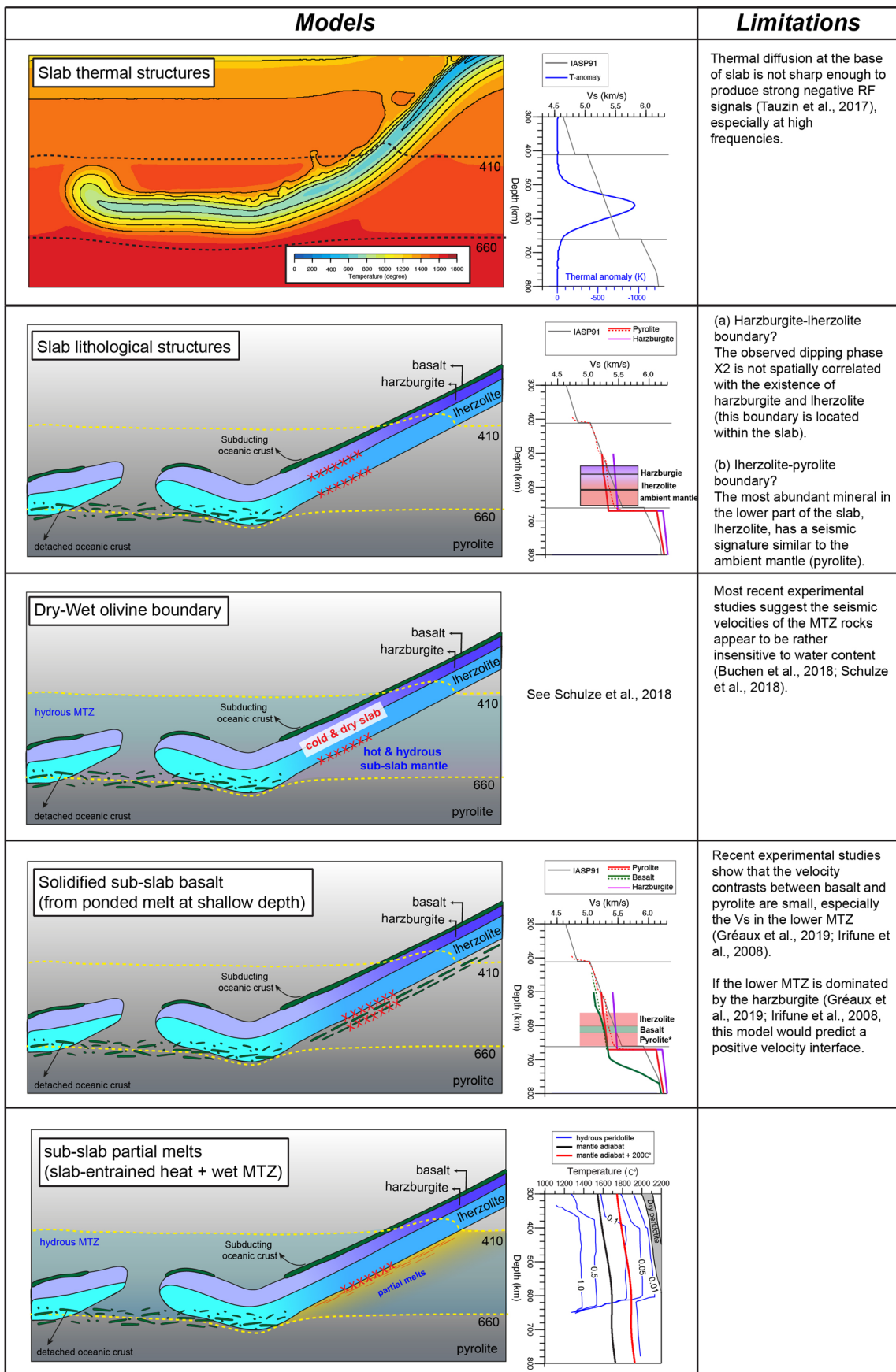
Extended Data Fig. 6 | Multi-frequency receiver function waveform modeling results for both the synthetic data and observation. a–f, Diagrams show the variation of the amplitude of the Pds phase with transition thickness, velocity perturbation and Gaussian filter parameter. Black heavy line indicates the amplitude of the 410-km discontinuity in IASP91 model⁴⁹ for reference. **e–i,** The frequency dependent amplitude of the Pds phases in real data, along with the uncertainties estimated by a bootstrapping method.



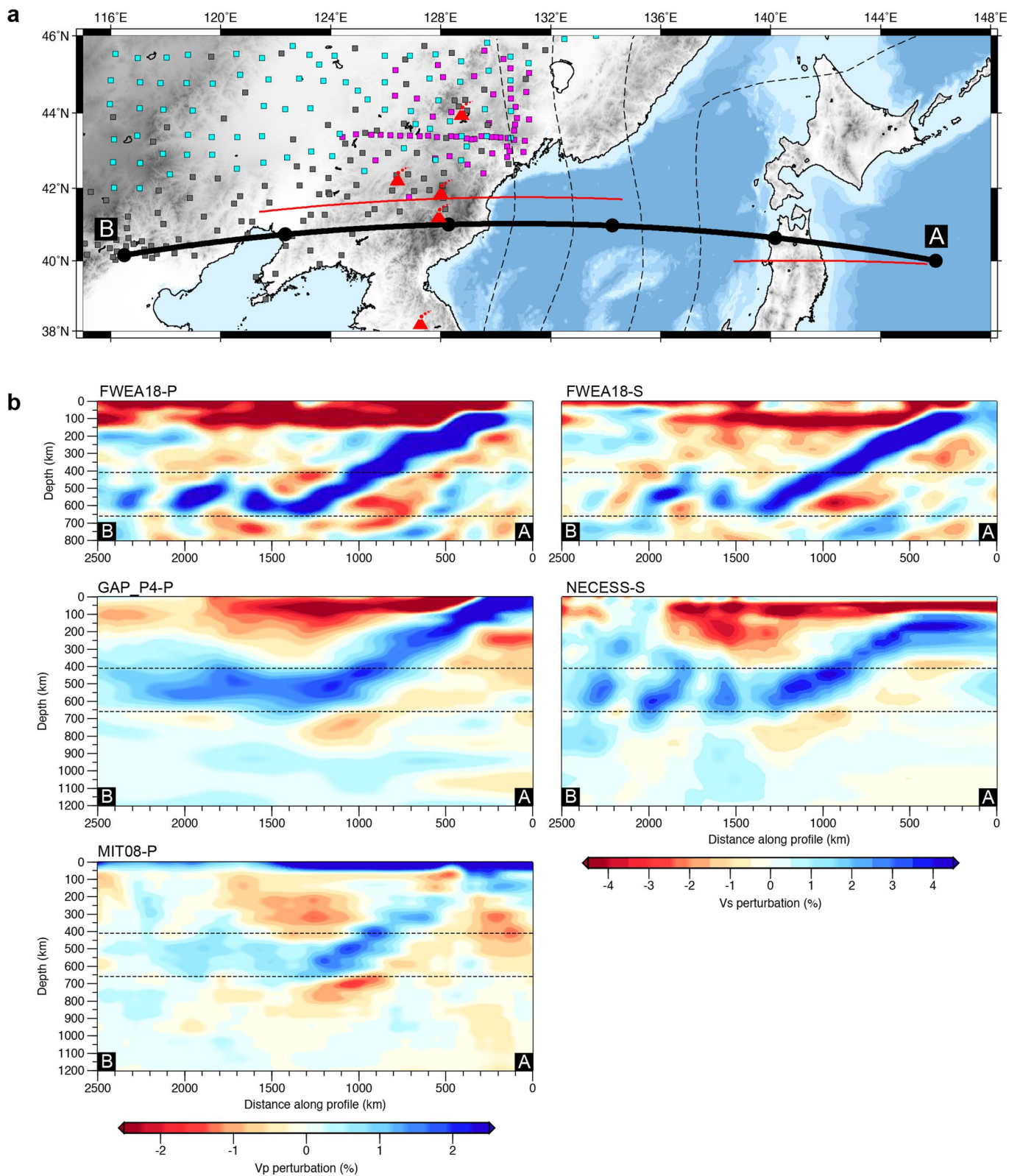
Extended Data Fig. 7 | Sensitivity test for the multi-frequency receiver function waveform modeling. **a**, and **b**, Examples show the multi-frequency Receiver Function (RF) waveforms sensitivity to the thickness and shear-wave speed. **c**, The RF waveforms are more sensitive to the relative velocity change along the depth, rather than the absolutely velocity value.



Extended Data Fig. 8 | Estimated topography of wadsleyite-ringwoodite phase transition based on thermal anomalies from tomography models. **a**, S-velocity model of FWEA18-S⁴, NECESS-S⁴¹ along the profile A shown in the main text. **b**, The estimated temperature anomaly using a temperature-velocity relationship²⁹ of $dV_s/T = -3.1 \times 10^{-4} \text{ km s}^{-1} \text{ K}^{-1}$. The thick red line shows the estimated temperature at 520 km depth. The thin gray lines show the estimated temperature profiles over a 100 km depth interval around 520 km to accompany the resolution of tomographic studies. **c**, Estimated topography of wadsleyite-ringwoodite phase transition using a Clapeyron slope of 2 MPa/K²³. The purple lines show the estimation, while the thick black line shows the observation. **d**, Similar as (c), but for a Clapeyron slope of 4 MPa/K²³. Note that even though the velocity anomalies in regions A and B are very similar in magnitude, the depths of observed phase X1 have a large difference.



Extended Data Fig. 9 | Comparison of different models for interpreting the observed Phase X2. Schematic cartoons show different models/interpretations (left column), while the limitations of each model are shown in the right column^{29,32,35,58,59}.



Extended Data Fig. 10 | Comparison of a variety of tomography models along a same profile. P-velocity model of FWEA18-P⁴, GAP_P4², MIT-08⁵⁰ and S-velocity model of FWEA18-S⁴, NECESS-S⁴¹. The general features, such as the high velocity anomaly interpreted as the subducting Pacific slab and the low velocity sub-slab anomalies, can be observed in all these models. However, the distribution and amplitude of these anomalies are different from each other. The FWEA18 is expected to have higher spatial resolution than the others in the northwest Pacific region, due to the dense seismic data coverage and the usage of full-waveform inversion algorithm⁴. Therefore, we use the FWEA18 model to conduct 3D velocity correction in our RF analysis.